

# A comprehensive chemical abundance analysis of the extremely metal poor Leoncino Dwarf galaxy (AGC 198691)

Erik Aver<sup>1</sup>, Danielle A. Berg<sup>2</sup>, Alec S. Hirschauer<sup>3</sup>, Keith A. Olive<sup>4,5,6</sup>, Richard W. Pogge<sup>7,8</sup>, Noah S. J. Rogers<sup>4,6</sup>, John J. Salzer<sup>9</sup>, Evan D. Skillman<sup>4,6</sup> <sup>★</sup>

<sup>1</sup>*Department of Physics, Gonzaga University, 502 E Boone Ave., Spokane, WA 99258*

<sup>2</sup>*Astronomy Department, University of Texas at Austin, Austin, TX 78712*

<sup>3</sup>*Space Telescope Science Institute, 3700 San Martin Drive, Baltimore, MD 21218*

<sup>4</sup>*School of Physics and Astronomy, University of Minnesota, 116 Church St. SE, Minneapolis, MN 55455*

<sup>5</sup>*William I. Fine Theoretical Physics Institute, University of Minnesota, 116 Church St. SE, Minneapolis, MN 55455*

<sup>6</sup>*Minnesota Institute for Astrophysics, University of Minnesota, 116 Church St. SE, Minneapolis, MN 55455*

<sup>7</sup>*Department of Astronomy, The Ohio State University, 140 W 18th Ave., Columbus, OH 43210*

<sup>8</sup>*Center for Cosmology & AstroParticle Physics, The Ohio State University, 191 West Woodruff Ave., Columbus, OH 43210*

<sup>9</sup>*Department of Astronomy, Indiana University, 727 East Third St., Bloomington, IN 47405*

2 September 2021

## ABSTRACT

We re-examine the extremely metal-poor (XMP) dwarf galaxy AGC 198691 using a high quality spectrum obtained by the LBT’s MODS instrument. Previous spectral observations obtained from KOSMOS on the Mayall 4-m and the Blue Channel spectrograph on the MMT 6.5-m telescope did not allow for the determination of sulfur, argon, or helium abundances. We report an updated and full chemical abundance analysis for AGC 198691, including confirmation of the extremely low “direct” oxygen abundance with a value of  $12 + \log(\text{O}/\text{H}) = 7.06 \pm 0.03$ . AGC 198691’s low metallicity potentially makes it a high value target for helping determine the primordial helium abundance ( $Y_p$ ). Though complicated by a Na I night sky line partially overlaying the He I  $\lambda 5876$  emission line, the LBT/MODS spectrum proved adequate for determining AGC 198691’s helium abundance. We employ the recently expanded and improved model of Aver et al. (2021), incorporating higher Balmer and Paschen lines, augmented by the observation of the infrared helium emission line He I  $\lambda 10830$  obtained by Hsyu et al. (2020). Applying our full model produced a reliable helium abundance determination, consistent with the expectation for its metallicity. Although this is the lowest metallicity object with a detailed helium abundance, unfortunately, due to its faintness ( $\text{EW}(\text{H}\beta) < 100 \text{ \AA}$ ) and the compromised He I  $\lambda 5876$ , the resultant uncertainty on the helium abundance is too large to allow a significant improvement on the measurement of  $Y_p$ .

**Key words:** galaxies: dwarf, galaxies: abundances, primordial nucleosynthesis

## 1 INTRODUCTION

### 1.1 Extremely Metal Poor Galaxies

Extremely metal-poor galaxies (XMPs) have been defined as galaxies with metal abundances roughly 5% of the solar value or less,  $12 + \log(\text{O}/\text{H}) \leq 7.35$  (Guseva et al. 2015; McQuinn et al. 2020). This definition has been adopted to characterize the most extreme systems amongst the growing number of metal poor galaxies known (McQuinn et al. 2020). These galaxies are of importance for studying the star formation process at low metallicity, which is relevant for understanding star formation in the early universe. Furthermore,

when an XMP galaxy hosts a high surface brightness H II region, then these galaxies can be used to determine the primordial helium abundance ( $Y_p$ ).

The number of actively star forming XMP galaxies remains small due to various limitations in our ability to identify them (see Sánchez Almeida et al. 2017). Following the analysis presented in McQuinn et al. (2020), to date, there appear to be two different formation channels for XMP galaxies. The first is simply the result of the relationship between a galaxy’s stellar-mass and its metallicity (e.g., Tremonti et al. 2004; Berg et al. 2012). This relationship implies that the most metal-poor galaxies are the least luminous, and therefore are difficult to identify in galaxy surveys. A second channel for XMP formation has been identified with the recent infall of relatively pristine gas onto a low mass galaxy (e.g., Ekta & Chengalur 2010). This infall results in a depression of the gas metallicity and this can drive a galaxy into the regime of XMP galaxies.

There has been recent progress in identifying XMP galaxies in both of these categories. For example, Skillman et al. (2013);

<sup>★</sup> e-mail addresses:

aver@gonzaga.edu, daberg@austin.utexas.edu, ahirschauer@stsci.edu,  
olive@umn.edu, pogge.1@osu.edu, roge0291@umn.edu,  
josalzer@indiana.edu, skill001@umn.edu

Hirschauer et al. (2016); Hsyu et al. (2018); James et al. (2017); Yang et al. (2017); Senchyna & Stark (2019); Senchyna et al. (2019); Kojima et al. (2020); Pustilnik et al. (2020) have all discovered XMP galaxies by obtaining spectra of inherently low luminosity galaxies. Izotov et al. (2012); Guseva et al. (2017); Izotov et al. (2018a) have identified very high surface brightness star forming regions in XMP galaxies that tend to be preferentially in the recent infall category.

The lower limit on the metallicity of a star forming region is also of interest in constraining our knowledge of the evolution of galaxies. The current record holder has been identified by Izotov et al. (2018a) to have an oxygen abundance of  $12 + \log(\text{O}/\text{H}) = 6.98$ , which corresponds to roughly 2% of the solar value (adopting a value of 8.69 Asplund et al. 2009).

## 1.2 The Primordial Helium Abundance

Among the element abundances observed in XMP galaxies,  $^4\text{He}$  offers a window into the physics of the early universe, as these abundances can be used to determine the primordial helium abundance and test standard big bang nucleosynthesis (SBBN) (Walker et al. 1991; Olive et al. 2000; Pisanti et al. 2008; Cyburt et al. 2016; Pitrou et al. 2018; Fields et al. 2020). With the cosmic microwave background (CMB) determination of the baryon density (Planck Collaboration et al. 2020), SBBN is effectively a parameter-free theory (Cyburt et al. 2002). The primary uncertainty in the SBBN calculation of the  $^4\text{He}$  abundance is the neutron mean life,  $\tau_n = 879.4 \pm 0.6$  s (Particle Data Group et al. 2020), and the predicted primordial abundance is  $Y_p = 0.2469 \pm 0.0002$  (Fields et al. 2020; Yeh et al. 2021), i.e., with less than 0.1% accuracy. In contrast, the accuracy of the predicted deuterium abundance is about 4%,  $\text{D}/\text{H} = (2.51 \pm 0.11) \times 10^{-5}$  (Yeh et al. 2021). If precise abundance measurements are available,  $^4\text{He}$  and SBBN can be used to probe the physics beyond the standard model (Cyburt et al. 2005), for example, new particle degrees of freedom, often scaled as the number of light neutrinos,  $N_\nu$ .

Currently, the primordial helium abundance,  $Y_p$  is best determined by fitting the helium abundances of individual objects, ideally XMP galaxies, versus a measurement of metallicity (e.g., oxygen), and extrapolating back to zero metallicity (Peimbert & Torres-Peimbert 1974).  $^4\text{He}$  abundance determinations come from measurements of emission line spectra of extragalactic H II regions. However, obtaining an abundance from these data requires careful modeling, and there are significant sources of potential systematic uncertainty (Olive & Skillman 2001, 2004; Peimbert et al. 2007; Izotov et al. 2007; Aver et al. 2010). The use of Monte Carlo methods helps evaluate the fit between the data and theoretical model and captures the uncertainties on the physical model parameters from that data lensed through the model (Aver et al. 2011). Aver et al. (2012) found that most of the available observations are statistically inconsistent with the models used to extract abundances and employed corresponding quality cuts on their datasets. Recently, other analyses have found similar inconsistencies (Fernández et al. 2019; Hsyu et al. 2020). Whether these incompatibilities are due to deficiencies in the model, or the data, or both, is an open question which can only be answered through obtaining new observations.

Aver et al. (2021) have addressed both the model and data in order to increase the accuracy of  $^4\text{He}$  abundance determinations. They improved the treatment of the collisional excitation of H I and of underlying stellar absorption, as well as the approach for the blended line He I  $\lambda 3889$  with H8, including its underlying absorption and radiative transfer. In conjunction, they also expanded the model to

utilize additional emission lines, not previously employed in helium abundance analyses.

The Large Binocular Telescope (LBT)'s Multi-Object Double Spectrograph (LBT/MODS, Pogge et al. 2010) allows for optical & near-IR spectrum from the UV atmospheric cutoff to  $1 \mu\text{m}$ . Enabled by the LBT/MODS spectrograph's higher resolution, higher sensitivity, and broader wavelength coverage, Aver et al. (2021) were able to employ previously unused weaker helium, higher Balmer, and NIR Paschen emission lines observed for the XMP galaxy Leo P. Based on the gains demonstrated in Aver et al. (2015) from the He I  $\lambda 10830$  emission line, the LBT Utility Camera in the Infrared (LUCI, Seifert et al. 2003) was used to obtain a near-IR spectrum, from  $0.95$  to  $1.35 \mu\text{m}$ , providing the high-impact He I  $\lambda 10830$  emission line. The combined effect of the model improvements, additional optical emission lines, and IR He I  $\lambda 10830$  emission line was to reduce the uncertainty on the helium abundance determination of Leo P by 70% (Aver et al. 2021), leading to an improvement in the uncertainty in  $Y_p$  of 15% (from  $Y_p = 0.2449 \pm 0.0040$  to  $0.2453 \pm 0.0034$ ) simply from a reanalysis and addition of a single object.

This work takes a similar approach for the XMP galaxy AGC 198691 (Hirschauer et al. 2016), leveraging a high-resolution LBT/MODS optical spectrum to incorporate higher Balmer and NIR Paschen emission lines, combined with a He I  $\lambda 10830$  measurement from Hsyu et al. (2020), to determine the helium abundance for AGC 198691. As was the case for Leo P (Aver et al. 2021), the benefits of our improved methodology are significant. The LBT/MODS spectrum allows for a confirmation of the extremely low oxygen abundance determination, as well as the first determination of the helium abundance of AGC 198691.

This paper is organized as follows. First, in Section 2, we provide new observational data from AGC 198691. An analysis of the new data is made in section 3. In §3.1, the electron temperature and corresponding abundances are derived.  $^4\text{He}$  requires different methodology. That methodology is presented and the helium abundance determined in §3.2. Finally, Section 4 offers a discussion of the results and further prospects for improvement.

## 2 NEW LBT OBSERVATIONS OF AGC 198691

### 2.1 Background

AGC 198691 was discovered in the wide-field, unbiased HI 21 cm ALFALFA survey (Giovanelli et al. 2005; Haynes et al. 2011). AGC 198691 was originally recognized as being a galaxy of interest through its inclusion in the Survey for H I in Extremely Low-mass Dwarfs (SHIELD) sample (Cannon et al. 2011). Optical spectroscopic observations of the lone H II region in AGC 198691 were first reported in Hirschauer et al. (2016). Three spectral observations were obtained. One using the KPNO Ohio State Multi-Object Spectrograph (KOSMOS) on the Mayall 4-m and two nights using the Blue Channel spectrograph on the MMT 6.5-m telescope. The oxygen abundance in AGC 198691 was measured to be  $12 + \log(\text{O}/\text{H}) = 7.02 \pm 0.03$  (Hirschauer et al. 2016), based on composite spectrum from two night's observations using the MMT. At the time of publication, this was the lowest metallicity XMP known.

Hsyu et al. (2018) subsequently obtained a spectrum of AGC 198691 (referred to as J0943+3326 in that work) with the Keck observatory LRIS instrument and derived an oxygen abundance of  $12 + \log(\text{O}/\text{H}) = 7.16 \pm 0.07$ . This confirmed AGC 198691 as an XMP galaxy, but raised questions about the record holder status. In

the interim, [Izotov et al. \(2018b\)](#) have discovered J0811+4730 with an oxygen abundance of  $12 + \log(\text{O}/\text{H}) = 6.98 \pm 0.02$ .

AGC 198691 has recently been observed with the Hubble Space Telescope by [McQuinn et al. \(2020\)](#). They determine a distance of  $12.1_{-3.4}^{+1.7}$  Mpc from the observation of the tip of the red giant branch with a resultant estimate of stellar mass of  $7.3 \times 10^5 M_{\odot}$ . This result implies that AGC 198691 is consistent with the stellar mass-metallicity relationship established by nearby galaxies ([Berg et al. 2012](#)), similar to Leo P ([Skillman et al. 2013](#); [McQuinn et al. 2015](#)). [McQuinn et al. \(2020\)](#) quoted  $12 + \log(\text{O}/\text{H}) = 7.12 \pm 0.04$ , based on a preliminary analysis of the observation reported in this work, but using an earlier version of the data reduction pipeline.

## 2.2 LBT Observations

After the MMT spectrum revealed the very low oxygen abundance of AGC 198691, we acquired an LBT observation in order to obtain a higher signal-to-noise spectrum and to detect weak emission lines over a larger wavelength range. A spectrum was obtained with the Multi-Object Double Spectrograph on the Large Binocular Telescope (LBT/MODS, [Pogge et al. 2010](#)) on 2015 December 6 under relatively clear skies and approximately  $1''$  seeing. The blue side of MODS1 covers a wavelength range of 3200 to 5650 Å with a  $400 \text{ l mm}^{-1}$  grating providing a resolution of  $2.4 \text{ \AA}$ . The red side of MODS1 covers a wavelength range of 5650 to 10000 Å with a  $250 \text{ l mm}^{-1}$  grating providing a resolution of  $3.4 \text{ \AA}$ . Bias frames, flat-field lamp images, and sky flats were obtained. We observed GD71 as the standard star with a  $5 \times 60''$  spectrophotometric slit mask near the parallactic angle. The sensitivity function is determined using the HST CALSPEC flux tables (e.g., [Bohlin 2010](#)) which extend further into the UV and Near-IR than the original [Oke \(1990\)](#) standard star fluxes.

A total exposure time of 120 minutes was obtained with the MODS1 spectrograph in six 20 minute exposures. The extraction window was chosen to optimize the signal-to-noise in the faintest emission lines but broad enough to ensure a high-fidelity, robust measurement ( $\sim 22 \text{ } 0.12''$  pixels). The spectrum is shown in Figure 1.

## 2.3 Emission line fluxes and reddening

We used the CHAOS project’s MODS standard reduction pipeline for calibration and extraction of the spectrum and for the measurement of the emission line fluxes (see [Berg et al. 2015](#); [Rogers et al. 2021](#)). The modsCCDRed Python programs bias subtract and flat-field the input science, standard star, and calibration lamp images. Sky subtraction and region extraction is performed using the mod-sIDL reduction pipeline<sup>1</sup>, which operates in the XIDL reduction package<sup>2</sup>. Additionally, this pipeline uses the arc lamp images to calculate a wavelength calibration for the 1D spectra and uses the standard star observations to determine the sensitivity function for flux calibration and correction for atmospheric extinction.

The emission line fluxes were measured in the extracted one-dimensional spectrum by fitting Gaussian profiles. In cases where emission lines were blended, multiple Gaussian profiles were fit to derive the integrated line fluxes. The errors of the flux measurements

were approximated using

$$\sigma_{\lambda} \approx \sqrt{(2 \times \sqrt{N} \times \zeta)^2 + (0.02 \times F_{\lambda})^2}, \quad (1)$$

where  $N$  is the number of pixels spanning the Gaussian profile fit to the narrow emission lines, and  $\zeta$  is the rms noise in the continuum, determined as the average of the rms on each side of an emission line. For weak lines, the uncertainty is dominated by error from the continuum subtraction, so the rms noise term determines the uncertainty. For the lines with flux measurements much stronger than the rms noise of the continuum, the error is dominated by the flux calibration. A minimum flux uncertainty of 2% was assumed, based on the uncertainties in the standard star measurements ([Oke 1990](#)), and, for the strongest emission lines, it dominates the uncertainty estimate.

The relative intensities of the Balmer lines are used to solve for the reddening using the reddening law of [Cardelli et al. \(1989\)](#), assuming  $A_V = 3.1 E(B - V)$  and the theoretical case B values from [Storey & Hummer \(1995\)](#) interpolated to the temperature derived from the [O III] lines. We used a minimized  $\chi^2$  approach to solve simultaneously for the reddening and underlying absorption based on the  $\text{H}\alpha/\text{H}\beta$ ,  $\text{H}\gamma/\text{H}\beta$ , and  $\text{H}\delta/\text{H}\beta$  ratios (see [Olive & Skillman 2001](#)). The solution was consistent with an underlying Balmer absorption with equivalent width of  $1.5_{-0.4}^{+0.4} \text{ \AA}$ .

The reddening corrected emission line intensities, normalized to  $\text{H}\beta$  are presented in Table 1. Note that, due to the larger aperture size, higher spectral resolution, and extended wavelength coverage in the red, the LBT spectrum has allowed the detection of many additional faint and red emission lines. We have reported line intensities for some faint lines that are marginally detected ( $s/n < 3$ ) as they may be valuable for planning future spectroscopic observations.

The reddening correction can be tested by comparing the corrected higher numbered Balmer lines to their theoretical values. The  $\text{H}9 \lambda 3935$  and  $\text{H}10 \lambda 3798$  corrected fluxes are consistent with their theoretical ratios to  $\text{H}\beta$  of 0.074 and 0.054, respectively. The derived values are listed in Table 1. Note that in Section 3.2.2 we re-derive the reddening (and other parameters) from the combination of H and He lines and that the two derived values are in excellent agreement. The value derived here,  $C(\text{H}\beta) = 0.13 \pm 0.03$ , while small, is significantly larger than previous determinations ( $0.04 \pm 0.05$  from the MMT observations and 0.001 from the Keck observations). At a high Galactic latitude ( $b = 49.3^\circ$ ), with a corresponding expected foreground reddening value of  $C(\text{H}\beta) = 0.02$  ([Schlafly & Finkbeiner 2011](#)), and an extremely low metallicity, this might appear to be unexpectedly large. However, some degree of reddening is expected in any actively star forming region. The amplitude of the reddening correction does not have a large impact on the derived chemical abundances, but this discrepancy from previous observations is worth noting.

## 2.4 The He I $\lambda 5876$ emission line

Due to AGC 198691’s velocity ( $514 \text{ km s}^{-1}$ ) and the  $1''$  width of the LBT/MODS slit, the He I  $\lambda 5876$  emission line partially overlapped with the Na I  $\lambda 5889.95$  night sky emission line. The potential interference of the Na I D lines with He I  $\lambda 5876$  and the role that it plays in deriving He abundances was highlighted by [Davidson & Kinman \(1985\)](#) and [Dinerstein & Shields \(1986\)](#). The strong Na I atmospheric emission can complicate the subtraction of the night sky from the target spectrum, but there is also the possibility of absorption from

<sup>1</sup> <http://www.astronomy.ohio-state.edu/MODS/Software/modsIDL/>

<sup>2</sup> <https://www.ucolick.org/~xavier/IDL/>

<sup>3</sup> line flux of  $\text{H}\beta$  in units of  $10^{-16} \text{ erg s}^{-1} \text{ cm}^{-2}$

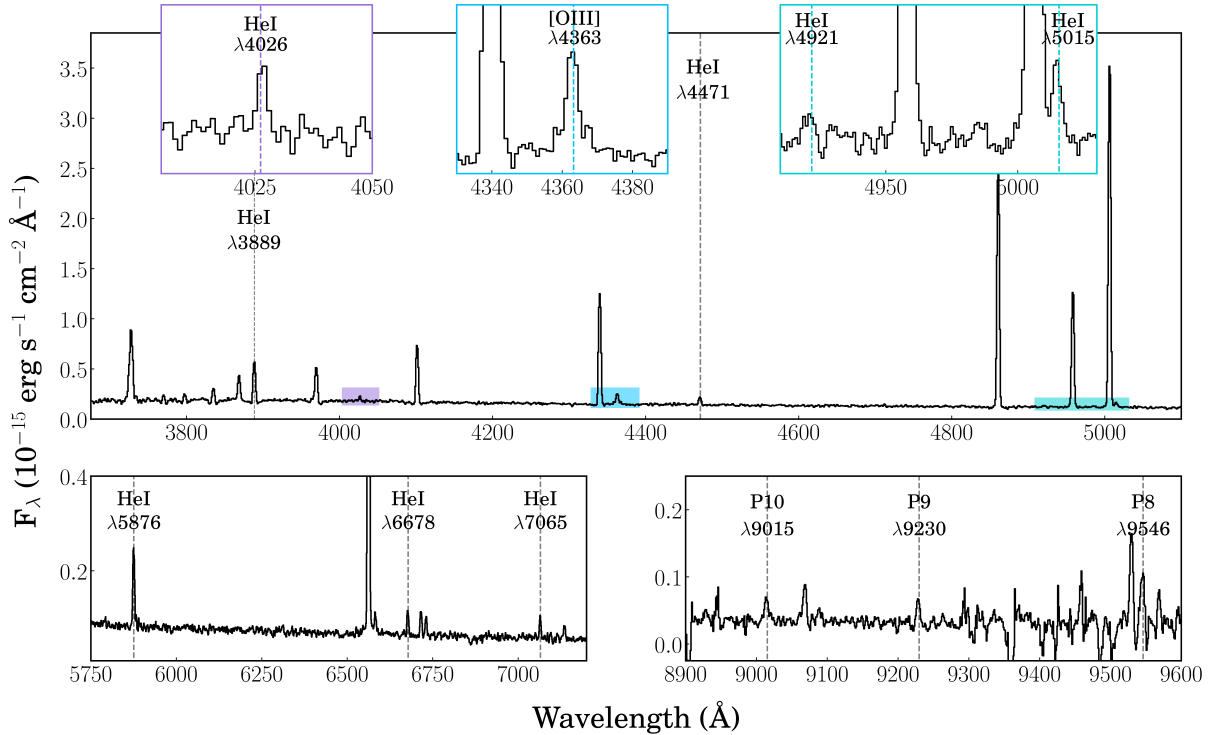


**Figure 1.** New LBT spectrum of AGC 198691 emphasizing weaker emission lines critical to the reported abundance analysis. Specifically, O III  $\lambda 4363$  allowing a temperature measurement for a direct oxygen abundance and several He I and H I emission lines which are used to solve for the reddening, radiative transfer, physical conditions, and helium abundance simultaneously.

the intervening Galactic neutral interstellar medium. For these reasons, Olive & Skillman (2004) proposed screening out targets used for the determination of  $Y_p$  in the heliocentric velocity ranges of  $728 \pm 100$  and  $1032 \pm 100$  km s $^{-1}$ . Of course, those ranges can be affected by the spectral resolution of the observations. Note that this screen is not applied uniformly across all determinations of  $Y_p$  in the literature. AGC 198691, with a radial velocity of 514 km s $^{-1}$ , would appear to be safely outside of this range, but our LBT spectrum reveals otherwise. Thus, a more conservative range of  $\pm 200$  km s $^{-1}$  may be appropriate.

Sky subtraction in the modsIDL pipeline is accomplished by fitting night sky emission lines with a B-spline in the dispersion direction and a low-order polynomial in the slit direction (Kelson 2003). He I  $\lambda 5876$  is the strongest optical helium emission line, and it carries corresponding importance in our analysis. As a result, without He I  $\lambda 5876$ , the precision of our helium abundance determination for AGC 198691 would be significantly reduced, and the reliability of the results suspect. Therefore, extracting a reliable measurement for He I  $\lambda 5876$  was a high priority. Luckily, only the higher-wavelength side of the emission line was clipped by the night sky line, which assisted in assessing the quality of the sky subtraction.

To extract a reliable He I  $\lambda 5876$ , the extraction window and sky subtraction regions were chosen to optimize the extraction of He I  $\lambda 5876$ , as well as the rest of the spectrum. The extraction was chosen to optimize both the signal-to-noise measure for the line, as well as the symmetry of the line profile. As mentioned in §2.2, a 22 pixel extraction window was employed, along with symmetrically chosen sky regions. The measured He I  $\lambda 5876/H\beta$  flux ratio is reported in the next section (§2.5) in Table 2, along with the other He and H lines used in our helium abundance analysis.

## 2.5 H and He Emission Line Fluxes and Equivalent Widths

In Table 2, we present the emission line fluxes, equivalent widths, and their associated uncertainties for all of the H and He recombination lines necessary for the helium abundance analysis of AGC 198691. The uncertainties on the flux measurements were approximated using equation 1.

The He I  $\lambda 10830$  emission line for AGC 198691 was observed by Hsyu et al. (2020) using Keck NIRES. It is reported as J0943+3326 after being independently identified by Hsyu et al. (2018). Given the utility of this emission line for helium abundance determinations (Izotov et al. 2014; Aver et al. 2015), we are very thankful to have this observation from Hsyu et al. (2020) for our analysis.

## 3 RESULTS

### 3.1 Physical Conditions and Elemental Abundances

#### 3.1.1 Electron Temperature and Density Determinations

For the purpose of deriving nebular abundances, we adopt a three zone approximation, where  $t_2$ ,  $t(S^{2+})$ , and  $t_3$  are the electron temperatures (in units of  $10^4$  K) in the low, intermediate, and high ionization zones respectively. For the high ionization zone, the [O III]  $I(\lambda\lambda 4959, 5007)/I(\lambda 4363)$  ratio was used to derive a temperature. We use PYNEB (Luridiana et al. 2012, 2015) to calculate the best-fit electron temperature from the measured auroral-to-nebular line flux ratio and using a density of  $n_e = 10^2$  cm $^{-3}$ . The derived temperature is given in Table 3. We derive a relatively high temperature of  $19,680 \pm 790$  K from the LBT/MODS spectrum, as expected for a low metallic-



**Table 1.** Emission-Line Intensity Ratios Relative to H $\beta$  for AGC 198691

| Ion                        | $\lambda$ [Å] | MMT 6.5-m (composite) | LBT           |
|----------------------------|---------------|-----------------------|---------------|
| H 14                       | 3721          | ...                   | 0.023±0.002   |
| [O II]                     | 3727.53       | 0.468 ± 0.025         | 0.429±0.027   |
| H 13                       | 3734          | ...                   | 0.029±0.003   |
| H 12                       | 3750.15       | ...                   | 0.035±0.011   |
| H 11                       | 3770.63       | ...                   | 0.039±0.011   |
| H 10                       | 3797.90       | ...                   | 0.046±0.025   |
| He I                       | 3819.64       | ...                   | 0.015±0.004   |
| H 9                        | 3835.39       | 0.053 ± 0.004         | 0.072±0.023   |
| [Ne III]                   | 3868.75       | 0.097 ± 0.006         | 0.114±0.006   |
| He I + H8                  | 3888.65       | 0.168 ± 0.009         | 0.209±0.016   |
| [Ne III] + H7              | 3969.56       | 0.176 ± 0.009         | 0.206±0.022   |
| He I                       | 4026.29       | ...                   | 0.025±0.005   |
| [S II]                     | 4068.60       | ...                   | 0.010±0.004   |
| [S II]                     | 4076.35       | ...                   | 0.008±0.005   |
| H $\delta$                 | 4101.74       | 0.254 ± 0.011         | 0.262±0.012   |
| He I                       | 4120.86       | ...                   | 0.007±0.003   |
| He I                       | 4143.76       | ...                   | 0.005±0.003   |
| H $\gamma$                 | 4340.47       | 0.482 ± 0.017         | 0.486±0.016   |
| [O III]                    | 4363.21       | 0.039 ± 0.003         | 0.046±0.004   |
| He I                       | 4387.93       | ...                   | 0.002±0.003   |
| He I                       | 4471.50       | 0.030 ± 0.003         | 0.036±0.003   |
| H $\beta$                  | 4861.33       | 1.000 ± 0.029         | 1.000±0.030   |
| He I                       | 4921.93       | 0.007 ± 0.002         | 0.010±0.002   |
| [O III]                    | 4958.91       | 0.418 ± 0.013         | 0.473±0.022   |
| [O III]                    | 5006.84       | 1.283 ± 0.037         | 1.386±0.065   |
| He I                       | 5016          | ...                   | 0.024±0.036   |
| [N II]                     | 5754.52       | ...                   | 0.003±0.002   |
| He I                       | 5875.62       | 0.075 ± 0.004         | 0.105±0.007   |
| [S III]                    | 6312.10       | ...                   | 0.008±0.003   |
| [N II]                     | 6548.03       | ...                   | 0.003±0.002   |
| H $\alpha$                 | 6562.82       | 2.758 ± 0.137         | 2.766±0.082   |
| [N II]                     | 6583.41       | 0.016 ± 0.002         | 0.017±0.002   |
| He I                       | 6678.15       | 0.023 ± 0.002         | 0.030±0.003   |
| [S II]                     | 6716.47       | 0.037 ± 0.003         | 0.031±0.003   |
| [S II]                     | 6730.85       | 0.031 ± 0.003         | 0.023±0.003   |
| He I                       | 7065.28       | ...                   | 0.025±0.002   |
| [Ar III]                   | 7135.78       | ...                   | 0.015±0.002   |
| [O II]                     | 7319.65       | ...                   | 0.008±0.002   |
| [O II]                     | 7330.16       | ...                   | 0.006±0.002   |
| [Ar III]                   | 7750.60       | ...                   | 0.011±0.005   |
| P 11                       | 8862.79       | ...                   | 0.019±0.010   |
| P 10                       | 9014.91       | ...                   | 0.023±0.003   |
| [S III]                    | 9068.90       | ...                   | 0.028±0.004   |
| P 9                        | 9229.02       | ...                   | 0.020±0.003   |
| [S III]                    | 9531.00       | ...                   | 0.066±0.010   |
| P 8                        | 9546.20       | ...                   | 0.040±0.011   |
| <hr/>                      |               |                       |               |
| c(H $\beta$ )              |               | 0.040 ± 0.053         | 0.137 ± 0.029 |
| EW(H $\beta$ )             |               | 64.3 Å                | 78.2 Å        |
| F(H $\beta$ ) <sup>3</sup> |               | 9.25 ± 0.19           | 9.65 ± 0.19   |

ity H II region and in good agreement with the temperature obtained from the MMT composite spectrum of [Hirschauer et al. \(2016\)](#).

Because neither the [O II]  $\lambda\lambda$ 7320,7320 lines nor the [N II]  $\lambda$ 5755 line were detected at high significance, we cannot derive a temperature for the low ionization zone directly and, therefore, need to assume a temperature. We used the  $T_e$ - $T_e$  relations proposed by [Pagel et al. \(1992\)](#), based on the photoionization modeling of [Stasińska \(1990\)](#) to determine the low ionization zone temperature:

$$t_2^{-1} = 0.5((t_3)^{-1} + 0.8). \quad (2)$$

**Table 2.** H and He Emission Line Fluxes and Equivalent Widths for AGC 198691

| Ion  | F( $\lambda$ )/F(H $\beta$ )  | W( $\lambda$ ) [Å] |
|--|-------------------------------|--------------------|
| H11 $\lambda$ 3771   | 0.0145 ± 0.0051               | 0.74               |
| H10 $\lambda$ 3798   | 0.0223 ± 0.0036               | 1.15               |
| H9 $\lambda$ 3835  | 0.0393 ± 0.0053               | 1.96               |
| He I+H8 $\lambda$ 3889   | 0.1515 ± 0.0054               | 7.71               |
| He I $\lambda$ 4026  | 0.0125 ± 0.0036               | 0.65               |
| H $\delta$ $\lambda$ 4101  | 0.2200 ± 0.0075               | 12.27              |
| H $\gamma$ $\lambda$ 4340  | 0.4457 ± 0.0134               | 28.26              |
| He I $\lambda$ 4471  | 0.0307 ± 0.0037               | 2.05               |
| H $\beta$ $\lambda$ 4861   | 1.0000 ± 0.0290               | 77.37              |
| He I $\lambda$ 5015  | 0.0215 ± 0.0033               | 1.76               |
| He I $\lambda$ 5876  | 0.1114 ± 0.0045               | 12.82              |
| H $\alpha$ $\lambda$ 6563  | 3.1031 ± 0.0890               | 435.0              |
| He I $\lambda$ 6678  | 0.0322 ± 0.0019               | 4.77               |
| He I $\lambda$ 7065  | 0.0249 ± 0.0035               | 3.98               |
| P10 $\lambda$ 9015   | 0.0209 ± 0.0034               | 5.79               |
| P9 $\lambda$ 9229  | 0.0227 ± 0.0040               | 7.27               |
| P8 $\lambda$ 9546  | 0.0481 ± 0.0141               | 14.69              |
| <hr/>  |                               | <hr/>              |
|  | F( $\lambda$ )/F(P $\gamma$ ) | W( $\lambda$ ) [Å] |
| He I $\lambda$ 10830   | 4.61053 ± 0.4232              | 58.20              |
| P $\gamma$ $\lambda$ 10940   | 1.00 ± 0.73                   | 5.29               |
| <hr/>  |                               |                    |
| F(H $\beta$ ) = (0.9539 ± 0.0196) × 10 <sup>-15</sup> erg s <sup>-1</sup> cm <sup>-2</sup> |                               |                    |

**Table 3.** Electron Temperatures & Densities and Ionic & Elemental Abundances

| Property   | MMT 6.5-m (composite) | LBT          |
|--|-----------------------|--------------|
| $T_e$ (O III) [K]                                    | 19130 ± 800           | 19680 ± 790  |
| $t_2$ (Inferred) [K]                                 | 15120 ± 560           | 15290 ± 550  |
| $t$ (S <sup>2+</sup> ) (Inferred) [K]                | ...                   | 16340 ± 830  |
| $n_e$ (S II) [cm <sup>-3</sup> ]                     | 270 ± 200             | 60 ± 220     |
| <hr/>  |                       |              |
| O <sup>+</sup> /H <sup>+</sup> [×10 <sup>6</sup> ]   | 3.11 ± 0.24           | 3.35 ± 0.43  |
| O <sup>++</sup> /H <sup>+</sup> [×10 <sup>6</sup> ]  | 7.35 ± 0.51           | 8.00 ± 0.71  |
| O/H [×10 <sup>6</sup> ]                              | 10.46 ± 0.68          | 11.35 ± 0.82 |
| 12+log(O/H)  | 7.02 ± 0.03           | 7.06 ± 0.03  |
| <hr/>  |                       |              |
| N <sup>+</sup> /H <sup>+</sup> [×10 <sup>7</sup> ]   | 0.95 ± 0.12           | 1.39 ± 0.20  |
| ICF (N)  | 3.37 ± 0.16           | 3.39 ± 0.50  |
| 12+log(N/H)  | 5.51 ± 0.06           | 5.67 ± 0.08  |
| log(N/O)   | -1.51 ± 0.06          | -1.38 ± 0.06 |
| <hr/>  |                       |              |
| Ne <sup>++</sup> /H <sup>+</sup> [×10 <sup>6</sup> ] | 1.22 ± 0.11           | 1.48 ± 0.16  |
| ICF (Ne)   | 1.42 ± 0.03           | 1.42 ± 0.16  |
| 12+log(Ne/H)   | 6.24 ± 0.04           | 6.32 ± 0.06  |
| log(Ne/O)  | -0.78 ± 0.02          | -0.73 ± 0.03 |
| <hr/>  |                       |              |
| S <sup>+</sup> /H <sup>+</sup> [×10 <sup>7</sup> ]   | ...                   | 0.55 ± 0.05  |
| S <sup>++</sup> /H <sup>+</sup> [×10 <sup>7</sup> ]  | ...                   | 1.84 ± 0.32  |
| ICF (S)  | ...                   | 1.40 ± 0.14  |
| 12+log(S/H)  | ...                   | 5.52 ± 0.07  |
| log(S/O)   | ...                   | -1.53 ± 0.07 |
| <hr/>  |                       |              |
| Ar <sup>++</sup> /H <sup>+</sup> [×10 <sup>8</sup> ] | ...                   | 4.59 ± 0.76  |
| ICF (Ar)   | ...                   | 1.09 ± 0.11  |
| 12+log(Ar/H)   | ...                   | 4.70 ± 0.08  |
| log(Ar/O)  | ...                   | -2.35 ± 0.08 |

The [S III]  $\lambda 6312$  emission line was only detected at the  $2\text{-}\sigma$  level, so for the temperature in the [S III] zone we assumed a temperature based on the relationship derived by Garnett (1992):

$$t(S^{+2}) = 0.83(t_3) + 0.17. \quad (3)$$

To account for the uncertainties/shortcomings of  $T_e\text{-}T_e$  relations in accounting for real electron temperature variations, the uncertainty in the inferred  $t_2$  and  $t(S^{+2})$  is calculated as the addition of the uncertainty on  $t_3$  and 500 K in quadrature. The different ionization zone temperatures are tabulated in Table 3.

[S II]  $\lambda\lambda 6717, 6731$  and  $t_2$  were used to determine the electron density. This density is consistent with the low density limit, or  $n_e < 10^2 \text{ cm}^{-3}$ . As such, we assume  $n_e = 10^2 \text{ cm}^{-3}$  for all abundance calculations.

### 3.1.2 Oxygen and Nitrogen Abundance Determinations

We determine oxygen abundances based on our estimated ionization zone electron temperatures. Ionic abundances were calculated with:

$$\frac{N(X^i)}{N(H^+)} = \frac{I_{\lambda(i)} j_{H\beta}}{I_{H\beta} j_{\lambda(i)}}, \quad (4)$$

where the  $I$  values are the relative emission line intensities and the  $j$  values are the volume emissivities for the individual emission lines. The emissivities are functions of electron temperature within the ionization zone containing the specific ionic species. For the low-ionization species of  $N^+$ ,  $O^+$ , and  $S^+$ , we use  $t_2$ ; for high-ionization species such as  $O^{2+}$  and  $Ne^{2+}$ , we use the directly measured temperature from [O III]  $\lambda 4363$ , or  $t_3$ ; for  $S^{2+}$  and  $Ar^{2+}$ , we apply the inferred  $t(S^{+2})$ . To determine the abundances, we use PYNEB, assuming a five-level atom model (De Robertis et al. 1987), the updated atomic data used in Berg et al. (2015), the electron temperature of a given ionization zone, and assuming an electron density of  $10^2 \text{ cm}^{-3}$ . The total oxygen abundance, O/H, is the sum of  $O^+/H^+$  and  $O^{++}/H^+$ .

The oxygen abundance determination is given in Table 3. We derive an oxygen abundance of  $12 + \log(O/H) = 7.06 \pm 0.03$ . This value agrees well with the value derived by Hirschauer et al. (2016) of  $12 + \log(O/H) = 7.02 \pm 0.03$ .

As a result, the oxygen abundance in AGC 198691 is still one of the lowest oxygen abundances ever derived for an H II region. The oxygen abundance in AGC 198691 is less than that of I Zw 18 (with  $12 + \log(O/H) = 7.17 \pm 0.04$ ; Skillman & Kennicutt 1993; Izotov & Thuan 1999), SBS 0335-052E ( $\log(O/H) = 7.33 \pm 0.01$ ; Izotov et al. 1997), SBS 0335-052W ( $\log(O/H) = 7.12 \pm 0.03$ ; Izotov et al. 2005), and DDO 68 ( $\log(O/H) = 7.14 \pm 0.03$ ; Pustilnik et al. 2005; Izotov & Thuan 2007). However, it is formally less metal-poor than the current record holder J0811+4730 with an oxygen abundance of  $12 + \log(O/H) = 6.98 \pm 0.02$  (Izotov et al. 2018b).

We derive the N/O abundance ratio from the [O II]  $\lambda 3727$ /[N II]  $\lambda 6584$  ratio and assume  $N/O = N^+/O^+$  (Peimbert & Costero 1969). Nava et al. (2006) have investigated the validity of this assumption. They concluded that, although it could be improved upon with modern photoionization models, it is valid to within about 10%. The nitrogen to oxygen relative abundances are given in Table 3; the value for  $\log(N/O)$  determined from the LBT/MODS spectrum is  $-1.38 \pm 0.06$ .

The newly derived value of N/O in AGC 198691 is higher than the previous AGC 198691 determination from Hirschauer et al. (2016). It is also significantly higher than the very narrow plateau at  $-1.60 \pm 0.02$  which Izotov & Thuan (1999) highlighted in their study of very low metallicity emission line galaxies. However, it is comparable to

the value derived for Leo P ( $-1.36 \pm 0.04$ ) and the low metallicity isolated dwarf irregular galaxies observed by van Zee & Haynes (2006).

### 3.1.3 Neon, Sulfur, and Argon Abundances

To estimate the neon abundance, we assume that  $Ne/O = Ne^{++}/O^{++}$  (Peimbert & Costero 1969). The neon to oxygen relative abundance determinations are given in Table 3. We derive  $\log(Ne/O) = -0.73 \pm 0.03$ . This is in good agreement with the value observed in Leo P of  $-0.76 \pm 0.03$  (Skillman et al. 2013) and typical of values derived in other XMP galaxies (Izotov & Thuan 1999; Izotov et al. 2012).

To determine the sulfur and argon abundances, for direct comparison, we adopt ionization correction factors (ICF) from the literature. For sulfur, we use the ICF from Thuan et al. (1995) generated from H II region photoionization models to correct for the unobserved  $S^{+3}$ . To account for the  $Ar^{+2}$ , and  $Ar^{+4}$  states, we use [Ar III]  $\lambda 7135$  in conjunction with the low-metallicity ICF of Izotov et al. (2006). In both cases, we assume a 10% uncertainty when applying these ICFs. For  $\log(S/O)$  we obtain  $-1.53 \pm 0.07$ . This relative abundance agrees with the value found in Leo P of  $-1.49 \pm 0.07$ , and is comparable to the average of values reported for other XMP galaxies by Izotov & Thuan (1999); Izotov et al. (2012). For  $\log(Ar/O)$  we obtain  $-2.35 \pm 0.08$ . This is significantly lower than the value found for Leo P of  $-2.00 \pm 0.09$  but consistent with the range of  $\log(Ar/O)$  measured in other XMP galaxies found by Izotov & Thuan (1999); Izotov et al. (2012).

Overall the abundances of neon, sulfur, and argon are consistent with the trends for  $\alpha$  elements seen in low metallicity dwarfs, i.e., they appear to be constant as a function of metallicity (e.g., Thuan et al. 1995). This is easiest to understand as a result of a nearly universal stellar initial mass function and no strong dependence of nucleosynthetic yields on metallicity.

## 3.2 The Helium Abundance

### 3.2.1 Methodology

H II regions are emission nebulae photoionized by one or more massive stars (O & B stars). Correspondingly, their spectra include nebular emission lines overlaid on a stellar continuum. In seeking the helium abundance,  $y^+ = \frac{n(He\ II)}{n(H\ II)}$ , we model the primary emission region using a radiative transfer model based on the case B approximation (optically thick to Lyman lines). For hydrogen and helium, recombination emission dominates, but collisional excitation also contributes, with hydrogen collisional excitation from the small fraction of neutral hydrogen in the ionized region,  $\xi$ . Self-absorption and re-emission of photons within the nebula also occurs. The radiative transfer model assumes a uniform H II region with average electron density,  $n_e$ , and average electron temperature,  $T_e$ , as well as optical depth,  $\tau$ . The stellar continuum juxtaposes absorption features under the nebular helium and hydrogen emission lines, including separate parameters for the Balmer and Paschen lines (Aver et al. 2021),  $a_{He}$ ,  $a_H$ , and  $a_P$ , respectively. Dust along the line of sight also scatters the emitted photons (interstellar reddening,  $C(H\beta)$ ).

We determine the  $^4\text{He}$  abundance in an individual H II region based on a Markov Chain Monte Carlo (MCMC) analysis. The MCMC method is an algorithmic procedure for sampling from a statistical distribution (Markov 1906; Metropolis et al. 1953). We define a  $\chi^2$

distribution from the difference between flux ratios,

$$\chi^2 = \sum_{\lambda} \left( \frac{F(\lambda)}{F(H\beta|P\gamma)} - \frac{F(\lambda)}{F(H\beta|P\gamma)_{meas}} \right)^2 \frac{1}{\sigma(\lambda)^2}, \quad (5)$$

where the emission line fluxes,  $F(\lambda)$ , are measured and calculated for a set of H and He lines, and  $\sigma(\lambda)$  is the measured uncertainty in the flux ratio at each wavelength. The optical/near-IR emission line fluxes from the LBT/MODS spectrum are calculated relative to H $\beta$ , while the infrared flux He I  $\lambda$ 10830 from Hsyu et al. (2020) is calculated relative to the IR Paschen line, P $\gamma$ . Thus, by  $F(H\beta|P\gamma)$ , we mean  $F(H\beta)$  for all lines other than He I  $\lambda$ 10830, and  $F(P\gamma)$  for the latter.

For this work seven helium line ratios are employed:  $\lambda\lambda$ 4026, 4471, 5015, 5876, 6678, and 7065, relative to H $\beta$ , and  $\lambda$ 10830, relative to P $\gamma$ . Nine hydrogen line ratios are employed: H $\alpha$ , H $\gamma$ , H $\delta$ , H9, H10, H11, P8, P9, and P10, relative to H $\beta$ . Finally, the blended line He I  $\lambda$ 3889 + H8, relative to H $\beta$ , is also employed. Note that four lines ( $\lambda$ 4922, H12, P11, and P12) considered in Aver et al. (2021) are not used here as they are too faint to contribute, as can be seen from Table 1.

These observed line ratios are used to fit nine model parameters, as introduced above (Aver et al. 2021):  $T_e$ ,  $n_e$ ,  $\tau$ ,  $C(H\beta)$ ,  $a_{He}$ ,  $a_H$ ,  $a_P$ ,  $\xi$ , and  $y^+$ . Thus, we are left with 8 degrees of freedom, corresponding to a total of 17 observed line ratios and 9 parameters to fit.

The MCMC scans of our 9-dimensional parameter space map out the  $\chi^2$  distribution given above. We conduct a frequentist analysis, and the  $\chi^2$  is minimized to determine the best-fit solution for the nine physical parameters, including  $y^+$ , as well as determining the ‘‘goodness-of-fit’’. Uncertainties in each quantity are estimated by calculating a 1D marginalized likelihood and finding the 68% confidence interval from the increase in the  $\chi^2$  from the minimum. The model equations for the helium and hydrogen flux ratios are given in full and our entire model and the data employed are detailed in the extensive appendices in Aver et al. (2021).

### 3.2.2 The Helium Abundance

Using our expanded and updated model, as outlined in §3.2.1, and the new observations and measurements discussed in §2, AGC 198691 was analyzed using our MCMC analysis (Aver et al. 2011, 2021). The best-fit model parameter values and uncertainties are given in Table 4.

The helium abundance uncertainty is significantly larger than was observed for Leo P ( $y^+ = 0.0776^{+0.0057}_{-0.0032}$  vs.  $0.0823^{+0.0025}_{-0.0018}$ ) (Aver et al. 2021). Compared to Leo P, the larger relative uncertainties for the added hydrogen lines (and in particular compared to the three strongest hydrogen line ratios), limits their ability to constrain the solution. These larger relative uncertainties are due to the lower signal-to-noise for AGC 198691’s spectrum, compared to Leo P’s. AGC 198691 is a faint object ( $F(H\beta)$  is 3.5 times weaker), and this translates into lower signal-to-noise and increased uncertainties on the flux measurements. Similarly, the He I  $\lambda$ 10830 observation from Hsyu et al. (2020) carries a larger relative uncertainty than the corresponding observation for Leo P (9.18% vs. 3.18%). The helium mass fraction (used for the regression in §3.2.3) is  $Y = 0.2367 \pm 0.0132$ .

The reddening determined by our helium abundance model,  $0.13^{+0.02}_{-0.07}$ , is in excellent agreement with the  $0.14 \pm 0.03$  value found in our abundance analysis in Section 2.3. These are, of course, not fully independent determinations, but, since the helium abundance model involves many more model parameters and is based on only the helium and hydrogen emission lines, the agreement of these

**Table 4.** Physical conditions of AGC 198691 from H and He only

|                                 |                              |
|---------------------------------|------------------------------|
| Emission lines                  | 17                           |
| Free Parameters                 | 9                            |
| degrees of freedom              | 8                            |
| 95% CL $\chi^2$                 | 15.51                        |
| He <sup>+</sup> /H <sup>+</sup> | $0.0776^{+0.0057}_{-0.0032}$ |
| $n_e$ [cm <sup>-3</sup> ]       | $231^{+207}_{-159}$          |
| $a_{He}$ [Å]                    | $0.30^{+0.17}_{-0.16}$       |
| $\tau$                          | $0.00^{+0.55}_{-0.00}$       |
| $T_e$ [K]                       | $14,900^{+2000}_{-2600}$     |
| $C(H\beta)$                     | $0.13^{+0.02}_{-0.07}$       |
| $a_H$ [Å]                       | $1.69^{+0.21}_{-0.19}$       |
| $a_P$ [Å]                       | $0.97^{+0.60}_{-0.97}$       |
| $\xi \times 10^4$               | $0^{+402}_{-0}$              |
| $\chi^2$                        | 6.28                         |
| p-value                         | 62%                          |
| O/H $\times 10^5$               | $1.1 \pm 0.1$                |
| Y                               | $0.2367 \pm 0.0132$          |

results was not assured, and their consistency adds support to the robustness of the result. Similar to the value reported in 2.3, the value found here is also in agreement with the previous determination from Hirschauer et al. (2016) ( $0.04 \pm 0.05$ ), albeit primarily due to the relative large uncertainties on both values.

The physical solution looks reliable, with most best-fit physical parameters not constrained by their zero lower bound, and most of the parameter ranges (68% CI) also separated from zero. Along with our recent Leo P analysis (Aver et al. 2021), this helps bolster a conclusion from our first work incorporating He I  $\lambda$ 10830 (Aver et al. 2015). In our more recent analyses, employing more emission lines to better determine and constrain the physical model parameters, the best-fit parameter values reach their lower limits less frequently than in our preceding analyses (Aver et al. 2012, 2013). Correspondingly, the solutions more reliably report unambiguously valid physical values. In addition to the solution’s overall qualitative reliability, it should be noted that parameters reaching their physical lower limits reduces the uncertainties determined for all parameters (see Aver et al. (2011) and 1D marginalization for constructing parameter confidence intervals), which could then be viewed as underestimated. It is for this reason that it is important to assess the reliability of the physical solution based on its full parameter solution, as well as its best-fit  $\chi^2$  value.

Our physical solution for AGC 198691 fits 9 parameters using 17 emission line ratios. As indicated in Table 4, the total  $\chi^2$  for the best-fit solution was 6.22, for eight degree of freedoms, corresponding to a p-value of 62%. Note that the solutions for  $T_e$  &  $n_e$  found here, using our solution for  $y^+$ , are consistent with those listed in Table 3, derived from O III and S II, respectively. It should also be noted that  $T_e(\text{He II})$  is lower than  $T_e(\text{O III})$ , as expected. Table 5 provides a full comparison of the measured fluxes and the model predictions for AGC 198691, broken down by line. The relative uncertainty for each measured flux is also included. The stronger lines dominate the  $\chi^2$  minimization and best-fit solution, due to their lower relative uncertainties. However, the weaker lines, appropriately weighted by their larger uncertainties, still contribute to constrain the best-fit solution and parameter uncertainties. Of particular note, He I  $\lambda$ 5876 agrees well with its model-predicted flux (i.e., it agrees well with the other lines in their parameter determination). Its small  $\chi^2$  contribution (the second smallest of the optical helium lines)

**Table 5.** Comparison of the measured flux ratio to the model prediction by line for the best-fit solution for AGC 198691.

| Emission Line             | $\left(\frac{F(\lambda)}{F(H\beta)}\right)_{\text{meas}}$  | $\sigma$ | %     | $\left(\frac{F(\lambda)}{F(H\beta)}\right)_{\text{mod}}$  | $\chi^2$ |
|---------------------------|--|----------|-------|---|----------|
| <i>Helium:</i>            |  |          |       |   |          |
| He I $\lambda$ 4026       | 0.0125   | 0.0036   | 28.57 | 0.0104  | 0.333    |
| He I $\lambda$ 4471       | 0.0307   | 0.0037   | 12.07 | 0.0324  | 0.211    |
| He I $\lambda$ 5015       | 0.0215   | 0.0033   | 15.51 | 0.0231  | 0.210    |
| He I $\lambda$ 5876       | 0.1114   | 0.0045   | 4.04  | 0.1095  | 0.187    |
| He I $\lambda$ 6678       | 0.0322   | 0.0019   | 6.03  | 0.0317  | 0.078    |
| He I $\lambda$ 7065       | 0.0249   | 0.0035   | 14.00 | 0.0274  | 0.500    |
| <i>Hydrogen:</i>          |  |          |       |   |          |
| H11 $\lambda$ 3771        | 0.0145   | 0.0051   | 35.10 | 0.0117  | 0.320    |
| H10 $\lambda$ 3798        | 0.0223   | 0.0036   | 15.93 | 0.0229  | 0.025    |
| H9 $\lambda$ 3835         | 0.0393   | 0.0053   | 13.54 | 0.0396  | 0.003    |
| H $\delta$ $\lambda$ 4101 | 0.2200   | 0.0075   | 3.42  | 0.2218  | 0.056    |
| H $\gamma$ $\lambda$ 4340 | 0.4457   | 0.0134   | 3.01  | 0.4349  | 0.658    |
| H $\alpha$ $\lambda$ 6563 | 3.1031   | 0.0890   | 2.87  | 3.1096  | 0.005    |
| P10 $\lambda$ 9015        | 0.0209   | 0.0034   | 16.09 | 0.0182  | 0.624    |
| P9 $\lambda$ 9229         | 0.0227   | 0.0040   | 17.59 | 0.0270  | 1.150    |
| P8 $\lambda$ 9546         | 0.0481   | 0.0141   | 29.22 | 0.0402  | 0.314    |
| <i>Blended He+H:</i>      |  |          |       |   |          |
| He I+H8 $\lambda$ 3889    | 0.1515   | 0.0054   | 3.56  | 0.1532  | 0.101    |
|                           | $\left(\frac{F(\lambda)}{F(P\gamma)}\right)_{\text{meas}}$ | $\sigma$ | %     | $\left(\frac{F(\lambda)}{F(P\gamma)}\right)_{\text{mod}}$ | $\chi^2$ |
| He I $\lambda$ 10830      | 4.6105   | 0.4232   | 9.18  | 4.5763  | 0.007    |

provides support for the robustness of its extraction from the night-side emission line and its resulting reliability.

### 3.2.3 Relevance for the Primordial Helium Abundance

A regression of  $Y$ , the helium mass fraction, versus  $O/H$ , the oxygen abundance, from nearby galaxies, is used to extrapolate to the primordial value<sup>4</sup>. Besides AGC 198691, the  $O/H$  values are taken directly from [Izotov et al. \(2007\)](#), except for Leo P, where the value is taken from [Skillman et al. \(2013\)](#).

The relevant values for the objects other than AGC 198691 used in the regression are given [Aver et al. \(2021\)](#). The regression is based on the results from [Aver et al. \(2015\)](#), combined with the results for Leo P from [Aver et al. \(2021\)](#) and those for AGC 198691 from this work. There are 15 objects in the qualifying dataset of [Aver et al. \(2015\)](#), Leo P was added in [Aver et al. \(2021\)](#), and AGC 198691 is added to the previous results for those 16. Regression based on those 17 points yields

$$Y_p = 0.2448 \pm 0.0033, \quad (6)$$

with a slope of  $80 \pm 38$  and a total  $\chi^2$  of 8.1. The result is shown in [Fig. 2](#). This result for  $Y_p$  agrees well with the SBBN value of  $Y_p = 0.2469 \pm 0.0002$  ([Fields et al. 2020](#)), based on the Planck determined baryon density ([Planck Collaboration et al. 2020](#)). Eq. (6) also agrees well with the SBBN-independent, direct Planck estimation of  $Y_p = 0.239 \pm 0.013$  ([Planck Collaboration et al. 2020](#)), using temperature, polarization, and lensing data, which is not surprising given the relatively large uncertainty on the CMB measurement.

[Aver et al. \(2015\)](#) determined  $Y_p = 0.2449 \pm 0.0040$ , with a slope of  $79 \pm 43$ , and the addition of Leo P increased the precision to  $Y_p = 0.2453 \pm 0.0034$ , with a slope of  $75 \pm 39$  ([Aver et al. 2021](#)). Since

<sup>4</sup> This work takes  $Z = 20(O/H)$  such that  $Y = \frac{4y(1-20(O/H))}{1+4y}$

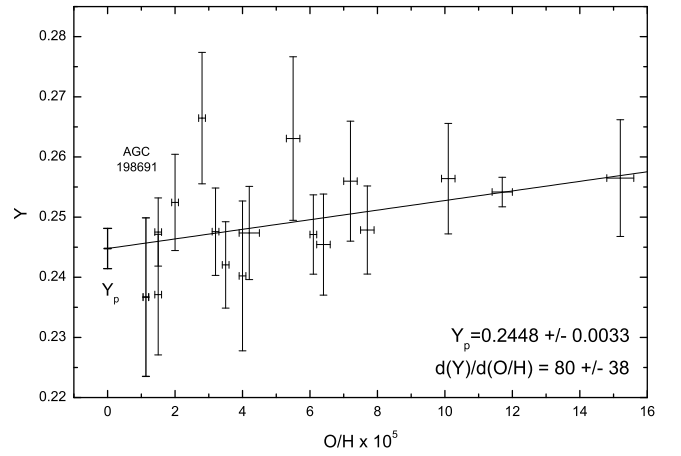


**Figure 2.** Helium abundance (mass fraction) versus oxygen to hydrogen ratio regression calculating the primordial helium abundance. The added point, AGC 198691, based on the analysis of this work, is shown as bold.

the result given in Eq. (6) is based on the same dataset, with only one additional point (AGC 198691), it is not surprising that the results are so similar. Furthermore, AGC 198691's larger uncertainty, due to its faintness, limits its ability to constrain the regression. Our result given in Eq. (6) is consistent with other recent determinations ([Valerdi et al. 2019](#); [Fernández et al. 2019](#); [Hsyu et al. 2020](#); [Kurichin et al. 2021](#)).

## 4 CONCLUSIONS

We have presented a new spectroscopic observation of the XMP dwarf galaxy, AGC 198691, taken by the LBT's MODS instrument. From this, we have reported an expanded chemical abundance analysis. Here we summarize our main findings and conclusions:

(i) The higher resolution and broader wavelength coverage afforded by LBT/MODS allowed for the first estimation of the sulfur, argon, and helium abundances for AGC 198691.

(ii) The oxygen abundance is in good agreement with the first determination for AGC 198691, as reported in [Hirschauer et al. \(2016\)](#), rather than the slightly higher value found by [Hsyu et al. \(2020\)](#).

(iii) This confirms AGC 198691 as one of the lowest metallicity galaxies ever discovered. Such XMP galaxies play a crucial role in studying and constraining models of chemical evolution and star formation and evolution in nearly pristine gas.

(iv) The abundances were broadly consistent with previous determinations ([Hirschauer et al. 2016](#)), though the spectral measurements showed an increased amount of reddening, with corresponding effects on the abundance results.

(v) Aided by the higher Balmer & Paschen lines enabled by LBT/MODS and a He I  $\lambda$ 10830 observation from [Hsyu et al. \(2020\)](#), we were able to apply our recently expanded and improved model ([Aver et al. 2021](#)) to determine the helium abundance for AGC 198691, with a well-determined full model parameter solution.

(vi) The faintness of AGC 198691 resulted in relatively large flux uncertainties and a corresponding large uncertainty on its helium abundance. As a result, even though AGC 198691 agreed well with its predicted helium abundance, based on our most recent regression analysis ([Aver et al. 2021](#)), its inclusion only very slightly reduced the uncertainty on the primordial helium abundance,  $Y_p$ .

(vii) This highlights that faint objects, even if extremely low



metallicity, have limited ability to improve the determination of the primordial helium abundance. Therefore, higher surface brightness objects should be prioritized, with both metallicity and surface brightness balanced as important selection criteria. Specifically, targets with  $EW(H\beta) > 200$  should be highest priority.

(viii) As evidenced by the robust results from our expanded helium abundance model, future observations of the most promising XMP galaxies, with high quality, high resolution, and broad wavelength coverage spectra, provide a uniquely promising route for improving the primordial helium abundance determination from observations of galaxies.

## ACKNOWLEDGEMENTS

The work of KAO is supported in part by DOE grant DE-SC0011842. EDS is grateful for partial support from the University of Minnesota. EA benefited greatly from three visits during sabbatical to the University of Minnesota and is grateful to the University of Minnesota and the William I. Fine Theoretical Physics Institute for the support.

This paper uses data taken with the MODS spectrographs built with funding from NSF grant AST-9987045 and the NSF Telescope System Instrumentation Program (TSIP), with additional funds from the Ohio Board of Regents and the Ohio State University Office of Research. This paper made use of the modsIDL spectral data reduction pipeline developed in part with funds provided by NSF Grant AST-1108693. This work was based in part on observations made with the Large Binocular Telescope (LBT). The LBT is an international collaboration among institutions in the United States, Italy and Germany. The LBT Corporation partners are: the University of Arizona on behalf of the Arizona university system; the Istituto Nazionale di Astrofisica, Italy; the LBT Beteiligungsgesellschaft, Germany, representing the Max Planck Society, the Astrophysical Institute Potsdam, and Heidelberg University; the Ohio State University; and the Research Corporation, on behalf of the University of Notre Dame, the University of Minnesota, and the University of Virginia. This research has made use of the NASA/IPAC Extragalactic Database (NED) which is operated by the Jet Propulsion Laboratory, California Institute of Technology, under contract with the National Aeronautics and Space Administration and the NASA Astrophysics Data System (ADS).

## REFERENCES

- Asplund M., Grevesse N., Sauval A. J., Scott P., 2009, *ARA&A*, 47, 481
- Aver E., Olive K. A., Skillman E. D., 2010, *J. Cosmology Astropart. Phys.*, 2010, 003
- Aver E., Olive K. A., Skillman E. D., 2011, *J. Cosmology Astropart. Phys.*, 2011, 043
- Aver E., Olive K. A., Skillman E. D., 2012, *J. Cosmology Astropart. Phys.*, 2012, 004
- Aver E., Olive K. A., Porter R. L., Skillman E. D., 2013, *J. Cosmology Astropart. Phys.*, 2013, 017
- Aver E., Olive K. A., Skillman E. D., 2015, *J. Cosmology Astropart. Phys.*, 2015, 011
- Aver E., Berg D. A., Olive K. A., Pogge R. W., Salzer J. J., Skillman E. D., 2021, *J. Cosmology Astropart. Phys.*, 2021, 027
- Berg D. A., et al., 2012, *ApJ*, 754, 98
- Berg D. A., Skillman E. D., Croxall K. V., Pogge R. W., Moustakas J., Johnson-Groh M., 2015, *ApJ*, 806, 16
- Bohlin R. C., 2010, *AJ*, 139, 1515
- Cannon J. M., et al., 2011, *ApJ*, 739, L22
- Cardelli J. A., Clayton G. C., Mathis J. S., 1989, *ApJ*, 345, 245
- Cybur R. H., Fields B. D., Olive K. A., 2002, *Astroparticle Physics*, 17, 87
- Cybur R. H., Fields B. D., Olive K. A., Skillman E., 2005, *Astroparticle Physics*, 23, 313
- Cybur R. H., Fields B. D., Olive K. A., Yeh T.-H., 2016, *Reviews of Modern Physics*, 88, 015004
- Davidson K., Kinman T. D., 1985, *ApJS*, 58, 321
- De Robertis M. M., Dufour R. J., Hunt R. W., 1987, *J. R. Astron. Soc. Canada*, 81, 195
- Dinerstein H. L., Shields G. A., 1986, *ApJ*, 311, 45
- Ekta B., Chengalur J. N., 2010, *MNRAS*, 406, 1238
- Fernández V., Terlevich E., Díaz A. I., Terlevich R., 2019, *MNRAS*, 487, 3221
- Fields B. D., Olive K. A., Yeh T.-H., Young C., 2020, *J. Cosmology Astropart. Phys.*, 2020, 010
- Garnett D. R., 1992, *AJ*, 103, 1330
- Giovanelli R., et al., 2005, *AJ*, 130, 2598
- Guseva N. G., Izotov Y. I., Fricke K. J., Henkel C., 2015, *A&A*, 579, A11
- Guseva N. G., Izotov Y. I., Fricke K. J., Henkel C., 2017, *A&A*, 599, A65
- Haynes M. P., et al., 2011, *AJ*, 142, 170
- Hirschauer A. S., et al., 2016, *ApJ*, 822, 108
- Hsyu T., Cooke R. J., Prochaska J. X., Bolte M., 2018, *ApJ*, 863, 134
- Hsyu T., Cooke R. J., Prochaska J. X., Bolte M., 2020, *ApJ*, 896, 77
- Izotov Y. I., Thuan T. X., 1999, *ApJ*, 511, 639
- Izotov Y. I., Thuan T. X., 2007, *ApJ*, 665, 1115
- Izotov Y. I., Lipovetsky V. A., Chaffee F. H., Foltz C. B., Guseva N. G., Kniazev A. Y., 1997, *ApJ*, 476, 698
- Izotov Y. I., Thuan T. X., Guseva N. G., 2005, *ApJ*, 632, 210
- Izotov Y. I., Stasińska G., Meynet G., Guseva N. G., Thuan T. X., 2006, *A&A*, 448, 955
- Izotov Y. I., Thuan T. X., Stasińska G., 2007, *ApJ*, 662, 15
- Izotov Y. I., Thuan T. X., Guseva N. G., 2012, *A&A*, 546, A122
- Izotov Y. I., Thuan T. X., Guseva N. G., 2014, *MNRAS*, 445, 778
- Izotov Y. I., Thuan T. X., Guseva N. G., Liss S. E., 2018a, *MNRAS*, 473, 1956
- Izotov Y. I., Thuan T. X., Guseva N. G., Liss S. E., 2018b, *MNRAS*, 473, 1956
- James B. L., Kopysov S. E., Stark D. P., Belokurov V., Pettini M., Olszewski E. W., McQuinn K. B. W., 2017, *MNRAS*, 465, 3977
- Kelson D. D., 2003, *PASP*, 115, 688
- Kojima T., et al., 2020, *ApJ*, 898, 142
- Kurichin O. A., Kislitsyn P. A., Klimenko V. V., Balashev S. A., Ivanchik A. V., 2021, *MNRAS*, 502, 3045
- Luridiana V., Morisset C., Shaw R. A., 2012, *IAU Symposium*, 283, 422
- Luridiana V., Morisset C., Shaw R. A., 2015, *A&A*, 573, A42
- Markov A. A., 1906, *Proc. Phys. Math. Soc. Kazan Univ.*, 15, 135
- McQuinn K. B. W., et al., 2015, *ApJ*, 812, 158
- McQuinn K. B. W., et al., 2020, *ApJ*, 891, 181
- Metropolis N., Rosenbluth A. W., Rosenbluth M. N., Teller A. H., Teller E., 1953, *J. Chem. Phys.*, 21, 1087
- Nava A., Casebeer D., Henry R. B. C., Jevremovic D., 2006, *ApJ*, 645, 1076
- Oke J. B., 1990, *AJ*, 99, 1621
- Olive K. A., Skillman E. D., 2001, *New Astron.*, 6, 119
- Olive K. A., Skillman E. D., 2004, *ApJ*, 617, 29
- Olive K. A., Steigman G., Walker T. P., 2000, *Phys. Rep.*, 333, 389
- Pagel B. E. J., Simonson E. A., Terlevich R. J., Edmunds M. G., 1992, *MNRAS*, 255, 325
- Particle Data Group et al., 2020, *Progress of Theoretical and Experimental Physics*, 2020, 083C01
- Peimbert M., Costero R., 1969, *Boletín de los Observatorios Tonantzintla y Tacubaya*, 5, 3
- Peimbert M., Torres-Peimbert S., 1974, *ApJ*, 193, 327
- Peimbert M., Luridiana V., Peimbert A., 2007, *ApJ*, 666, 636
- Pisanti O., Cirillo A., Esposito S., Iocco F., Manganò G., Miele G., Serpico P. D., 2008, *Computer Physics Communications*, 178, 956
- Pitrou C., Coc A., Uzan J.-P., Vangioni E., 2018, *Phys. Rep.*, 754, 1
- Planck Collaboration et al., 2020, *A&A*, 641, A6
- Pogge R. W., et al., 2010, in McLean I. S., Ramsay S. K., Takami H., eds, *Society of Photo-Optical Instrumentation Engineers (SPIE) Conference Series Vol. 7735, Ground-based and Airborne Instrumentation for Astronomy III*, p. 77350A. doi:10.1117/12.857215
- Pustilnik S. A., Kniazev A. Y., Pramskij A. G., 2005, *A&A*, 443, 91

- Pustilnik S. A., Kniazev A. Y., Perepelitsyna Y. A., Egorova E. S., 2020, *MNRAS*, **493**, 830
- Rogers N. S. J., Skillman E. D., Pogge R. W., Berg D. A., Moustakas J., Croxall K. V., Sun J., 2021, *ApJ*, **915**, 21
- Sánchez Almeida J., Filho M. E., Dalla Vecchia C., Skillman E. D., 2017, *ApJ*, **835**, 159
- Schlafly E. F., Finkbeiner D. P., 2011, *ApJ*, **737**, 103
- Seifert W., et al., 2003, in Iye M., Moorwood A. F. M., eds, Society of Photo-Optical Instrumentation Engineers (SPIE) Conference Series Vol. 4841, Instrument Design and Performance for Optical/Infrared Ground-based Telescopes. pp 962–973, doi:10.1117/12.459494
- Senchyna P., Stark D. P., 2019, *MNRAS*, **484**, 1270
- Senchyna P., Stark D. P., Chevallard J., Charlot S., Jones T., Vidal-García A., 2019, *MNRAS*, **488**, 3492
- Skillman E. D., Kennicutt Robert C. J., 1993, *ApJ*, **411**, 655
- Skillman E. D., et al., 2013, *AJ*, **146**, 3
- Stasińska G., 1990, *A&AS*, **83**, 501
- Storey P. J., Hummer D. G., 1995, *MNRAS*, **272**, 41
- Thuan T. X., Izotov Y. I., Lipovetsky V. A., 1995, *ApJ*, **445**, 108
- Tremonti C. A., et al., 2004, *ApJ*, **613**, 898
- Valerdi M., Peimbert A., Peimbert M., Sixtos A., 2019, *ApJ*, **876**, 98
- Walker T. P., Steigman G., Schramm D. N., Olive K. A., Kang H.-S., 1991, *ApJ*, **376**, 51
- Yang H., Malhotra S., Rhoads J. E., Wang J., 2017, *ApJ*, **847**, 38
- Yeh T.-H., Olive K. A., Fields B. D., 2021, *JCAP*, **03**, 046
- van Zee L., Haynes M. P., 2006, *ApJ*, **636**, 214